Article

On the RE_2TiAl$_3$ (RE = Y, Gd–Tm, Lu) Series—The First Aluminum Representatives of the Rhombohedral Mg$_2$Ni$_3$Si Type Structure

Elias C. J. Gießelmann [1] [ID], Stefan Engel [1] [ID], Israa M. El Saudi [1] [ID], Lars Schumacher [2], Mathis Radzieowski [2], Josef Maximilian Gerdes [2] [ID] and Oliver Janka [1,*] [ID]

[1] Anorganische Festkörperchemie, Universität des Saarlandes, Campus C4.1, 66386 Saarbrücken, Germany
[2] Institut für Anorganische und Analytische Chemie, Universität Münster, Corrensstrasse 28/30, 48149 Münster, Germany
[*] Correspondence: oliver.janka@uni-saarland.de; Tel.: +49-681-302-70665

Abstract: Several ternary rare-earth metals containing titanium aluminum intermetallics in the RE_2TiAl$_3$ series (RE = Y, Gd–Lu) have been synthesized from the elements using arc-melting techniques. All compounds crystallize in the trigonal crystal system with rhombohedral space group $R\bar{3}m$ (Z = 3) and lattice parameters ranging between a = 582–570 and c = 1353–1358 pm. They adopt the Mg$_2$Ni$_3$Si-type structure, which is an ordered superstructure of the cubic Laves phase MgCu$_2$ and has been observed for Al intermetallics for the first time. Tetrahedral [TiAl$_3$] entities that are connected over all corners form a network where the empty [TiAl$_3$] tetrahedra exhibit a full Ti/Al ordering based on the single crystal results. The Al atoms are arranged into 6^3 Kagomé nets, while the Ti atoms connect these nets over the triangular units. In the cavities of this three-dimensional arrangement, the RE cations can be found forming a distorted diamond-type substructure. Magnetic measurements revealed that Y$_2$TiAl$_3$ and Lu$_2$TiAl$_3$ are Pauli paramagnetic substances, in line with the metallic character. The other compounds exhibit paramagnetism with antiferromagnetic ordering at a maximum Néel temperature of T_N = 26.1(1) K for Gd$_2$TiAl$_3$.

Keywords: intermetallics; rare-earth elements; titanium; aluminum; physical properties

1. Introduction

The Laves phases of general composition AB_2, named after Fritz Laves, belong to the most prominent structure types in the field of intermetallic compounds [1–3]. The Pearson database [4] lists over 4000 (pseudo) binary compounds in the cubic MgCu$_2$ ($Fd\bar{3}m$) or the hexagonal MgZn$_2$ and MgNi$_2$ (both $P6_3/mmc$)-type structures [5]. The majority of these compounds contain a rare-earth element; therefore, the magnetic properties of these materials have been studied in great detail [6]. Their structures usually do not show larger homogeneity ranges and can be regarded as packing dominated as illustrated by the fact that, for example, NeHe$_2$ [7] and ArNe$_2$ [8] can be observed under high-pressure conditions and adopt the MgZn$_2$-type structure. Moreover, Ar(H$_2$)$_2$ was reported to form the hexagonal Laves phase at high pressure [9], while Xe(N$_2$)$_2$ adopts the cubic MgCu$_2$-type structure [10]. The ideal size ratio of the constituent elements A and B is $r_A/r_B = (3/2)^{1/2} \approx 1.225$. In all three binary Laves phases, the B atoms form empty B_4 tetrahedra that exhibit different connectivities, always forming a network, with the A atoms in the respective cavities. In the MgCu$_2$-type structure, however, only corner-sharing Cu$_4$ tetrahedra are present; in the MgZn$_2$-type structure, two tetrahedra are connected over a common face, and the remaining corners are used to form strands [001]. Finally, in MgNi$_2$, both connection modes can be found. In addition to these basic types, different (highly complex) stacking variants have been reported [11]. Based on these binary structure types, ordered ternary compounds can be derived. The Mg$_2$Cu$_3$Si ($P6_3/mmc$)-type structure [12],

for example, allows for an ordering on the two crystallographic Zn sites of the hexagonal $MgZn_2$-type structure. Besides the prototype, aluminum compounds (e.g., Ce_2RuAl_3 [13], the RE_2TAl_3 series with RE = Y, La–Nd, Sm, Gd–Lu and T = Ru, Rh, Ir [14], U_2Cu_3Al [15] or the solid solution $Ti_2Ni_{1-x}Al_{3+x}$ [16]) along with gallides (U_2Fe_3Ga [17], Eu_2IrGa_3 [18], $Nb_2Cu_{1.1}Ga_{2.9}$ [19], and $Ho_2Ru_2Ga_2$ [20]), silicides (e.g., the Sc_2T_3Si and Ti_2T_3Si series with T = Cr, Mn, Fe, Co, and Ni [21–23]), and germanides (U_2T_3Ge series with T = Mn, Fe, Co [24–27], Mn_2Cu_3Ge [28], and Mn_2Co_3Ge [29]) have been reported. The cubic $MgCu_4Sn$-type structure ($F\bar{4}3m$) [30] is a ternary ordered variant of the cubic $MgCu_2$ type, where magnesium/tin ordering takes place on the former Mg site. Exemplarily, the rare-earth-containing series $RENi_4In$ (RE = Sc, Y, La–Nd, Sm, Gd–Tm) [31], $RENi_4Au$ (RE = Sc, Y, Gd–Lu) [32,33], $RECu_4Ag$ (RE = La–Nd, Sm, Gd–Tm) [34], and $RECu_4Au$ (RE = Gd–Er) [35] should be mentioned. Furthermore, $Yb_6Ir_5Ga_7$ [36] represents a $\sqrt{3} \times \sqrt{3}$ superstructure of the hexagonal $MgZn_2$-type structure, allowing for a coloration of the tetrahedral strands of the prototype. To date, the iridium gallides $RE_6Ir_5Ga_7$ (RE = Sc, Y, Nd, Sm, Gd–Lu) [36,37] and the $RE_6T_5Al_7$ series (RE = Sc, Y, Ce–Nd, Sm, Gd–Lu, T = Ru, Ir) [38] have been reported. Finally, a rhombohedral ordered variant of the $MgCu_2$ type is observed for the Mg_2Ni_3Si ($R\bar{3}m$) type structure [39], realized, e.g., for the gallides RE_2Rh_3Ga (RE = Y, La–Nd, Sm, Gd–Er) [40], the silicides RE_2Rh_3Si (RE = Ce, Pr, Er) [41–43] and U_2Ru_3Si [44], or the germanides RE_2T_3Ge (RE = Y, Pr, Sm, Er) [41,45], U_2Ru_3Ge [44], and Ca_2Pd_3Ge [46]. More information on superstructures of the Laves phases can be found in a recent review article [47].

With respect to application, titanium and aluminum-based materials are of great interest since they belong to the group of light-weight alloys [48]. Therefore, the binary phase diagram Ti/Al is probably one of the best investigated ones [49–53]. Several binary intermetallics have been identified in this system, of which $TiAl_2$ and $TiAl_3$ are too brittle to be of technical importance; however, α_2-Ti_3Al and γ-$TiAl$ are of crucial importance to the field of titanium-based alloys [54,55].

Here, we report on the synthesis and structural and magnetic characterization of the RE_2TiAl_3 series (RE = Y, Gd–Tm, Lu), the first aluminum intermetallics adopting the rhombohedral Mg_2Ni_3Si-type structure. However, as seen for many aluminum series, they form an *anti*-type arrangement within the network in comparison to the [Ni_3Si] one, that is, the prototype.

2. Materials and Methods

Synthesis: The compounds of the RE_2TiAl_3 (RE = Y, Gd–Tm, Lu) series were synthesized by arc-melting the elements, using rare-earth ingots (Onyxmet, 99.9%), titanium chips (Onyxmet, 99.9%), and aluminum turnings (Onyxmet, 99.99%). All starting materials were weighed in the ideal stoichiometry of 2:1:3 (RE:Ti:Al). The reactants were arc-melted under an argon atmosphere of about 800 mbar [56]. The obtained buttons were remelted several times to increase the homogeneity. All samples were weighed after arc-melting; the mass loss is <0.5%. The samples were subsequently enclosed in evacuated quartz tubes and annealed in a second step (923 or 1123 K, 7 to 12 d) to increase their overall phase purity and homogeneity. The Tm_2TiAl_3 sample was transferred to an Al_2O_3 crucible and annealed for 3 h in an induction furnace (Trumpf Hüttinger, TruHeat 5010, Freiburg, Germany). The annealing led to X-ray pure samples, suitable for physical property measurements. All samples obtained by these processes show metallic luster and are stable under ambient conditions over months.

SEM-EDX data: Semiquantitative EDX analyses of the bulk samples were conducted on a JEOL 7000F (Jeol, Freising, Germany) equipped with an EDAX Genesis 2000 EDX detector (EDAX, Unterschleissheim, Germany). Investigations of the single crystals were conducted on a Zeiss Evo MA10 (Zeiss, Jena, Germany) scanning electron microscope with an Oxford Instrument EDX detector using REF$_3$, TiO_2, and Al_2O_3 as internal standards. The crystals used for the structure determination were measured on their glass fibers in the variable pressure (VP) mode of the instrument under 60 Pa N_2 atmosphere.

X-Ray diffraction: The annealed polycrystalline samples were analyzed by powder X-ray diffraction. Powder X-ray diffraction (PXRD) patterns of the pulverized samples were recorded at room temperature on a D8-A25-Advance diffractometer (Bruker, Karlsruhe, Germany) in Bragg–Brentano θ-θ-geometry (goniometer radius 280 mm) with Cu Kα-radiation (λ = 154.0596 pm). A 12 μm Ni foil working as K$_\beta$ filter and a variable divergence slit were mounted at the primary beam side. A LYNXEYE detector with 192 channels was used at the secondary beam side. Experiments were carried out in a 2θ range of 6 to 130° with a step size of 0.013° and a total scan time of 1 h.

Small fragments of the annealed and crushed samples of Y_2TiAl_3, Gd_2TiAl_3, and Tb_2TiAl_3 were glued to thin quartz fibers using beeswax. The crystallite quality was checked by Laue photographs on a Buerger precession camera (white molybdenum radiation; imaging plate system, Fujifilm, BAS-READER 1800, Minato, Japan). Intensity data sets of suitable single crystals were collected at room temperature, either on an IPDS-II (graphite-monochromatized Mo$K\alpha$ radiation; λ = 0.71073 pm; oscillation mode) or on a Bruker D8 Venture diffractometer (graphite-monochromatized Mo$K\alpha$ radiation; λ = 0.71073 pm) equipped with a μ-focus source.

CCDCs 1939725-1939727 contain the supplementary crystallographic data for this paper. The data can be obtained free of charge from The Cambridge Crystallographic Data Centre via www.ccdc.cam.ac.uk/structures.

Physical property measurements: Annealed pieces of the respective X-ray pure RE_2TiAl_3 (RE = Y, Gd–Tm, Lu) samples were attached to the sample holder rod of a Vibrating Sample Magnetometer (VSM) using Kapton foil for measuring the magnetization $M(H,T)$ in a Quantum Design (San Diego, CA, USA) Physical Property Measurement System (PPMS). All samples were investigated in the temperature range of 2.5–300 K with applied external magnetic fields of up to 80 kOe.

3. Results and Discussion

3.1. Structure Refinement

The obtained single crystal data sets showed a rhombohedral lattice; space group $R\bar{3}m$ was found to be correct during the structure refinement. Isotypism to the Mg_2Ni_3Si-type structure was evident from both single crystal and powder X-ray diffraction experiments. Starting values for the structure refinement were obtained using the SuperFlip [57] program package, implemented in Jana2006 [58,59]. All atomic positions and anisotropic displacement parameters were subsequently refined, again using Jana2006. Occupancy parameters of all crystallographic sites were individually refined in separate series of least-squares refinements to check for the correct composition. No mixing, especially of Ti and Al, was observed. The final difference Fourier syntheses were contourless. Details on the measurements, refined atomic parameters, displacement parameters, and interatomic distances can be found in Tables 1–4.

3.2. SEM-EDX Data

EDX investigations of the bulk samples were carried out exemplarily on Er_2TiAl_3, Tm_2TiAl_3, and Lu_2TiAl_3. The experimentally determined averaged element ratios (Table 5) were obtained from five spot measurements and one area measurement and are in good agreement with the ideal compositions. The crystals of Y_2TiAl_3, Gd_2TiAl_3, and Tb_2TiAl_3 measured on the diffractometer were analyzed semi-quantitatively using a SEM in combination with EDX (Table 5). No impurity elements heavier than sodium (detection limit of the instrument) were observed. The experimentally determined averaged element ratios were obtained from five spot measurements and are in good agreement with the ideal compositions. Differences originate from the conchoidal fractures of the crystallites and the non-perfect perpendicular orientation of the crystals to the beam.

3.3. Crystal Chemistry

The rare-earth compounds of the RE_2TiAl_3 series (RE = Y, Gd–Tm, Lu) crystallize in the trigonal Mg_2Ni_3Si-type structure with space group $R\bar{3}m$ and Z = 3. The lattice parameters and unit cell volumes (Table 6) decrease from the gadolinium to the lutetium compound, as expected due to the lanthanide contraction (Figure 1, Table 6). Y_2TiAl_3 exhibits lattice parameters similar to those of Tb_2TiAl_3, in line with the comparable ionic radii of the trivalent cations (Y^{3+}: 106 pm; Tb^{3+} 104 pm; CN = 8 [60]). In Figure 2, a comparison of the Rietveld fit of the experimental diffraction pattern of Y_2TiAl_3 using the trigonal Mg_2Ni_3Si type and the cubic $MgCu_2$-type structure is shown. The rhombohedral distortion is easily visible in the diffraction patterns due to the splitting of the reflections (Figures S1–S6, Tables S1–S6).

Table 1. Crystallographic data and structure refinement information for Y_2TiAl_3, Gd_2TiAl_3, and Tb_2TiAl_3, space group $R\bar{3}m$, Z = 3, Mg_2Ni_3Si type determined from single crystal X-ray diffraction data. All data sets were collected at room temperature.

Formula	Y_2TiAl_3	Gd_2TiAl_3	Tb_2TiAl_3
CCDC number	1939725	1939727	1939726
Molar mass, g mol^{-1}	306.6	443.3	446.7
Lattice parameters		see Table 6	
Density calc., g cm^{-3}	4.04	5.77	5.90
Crystal size, μm	50 × 40 × 35	30 × 25 × 10	40 × 40 × 20
Diffractometer	IPDS-II	IPDS-II	Bruker CCD
Wavelength; λ, pm	Mo$K\alpha$; 71.073	Mo$K\alpha$; 71.073	Mo$K\alpha$; 71.073
Transmission ratio (min/max)	0.2943/0.4102	0.5295/0.7673	0.3054/0.5561
Detector distance, mm	60	70	40
Exposure time, min	10	30	0.167
Integr. param. A, B, EMS	14.0; −1.0; 0.030	16.0; −4.0; 0.030	–
$F(000)$, e	417	567	573
Range in hkl	±9; −8, +9, ±21	±8; ±8, ±20	±7; ±8, −17, +20
θ_{min}, θ_{max}, deg	4.4/34.9	4.4/33.3	4.4/32.0
Linear absorption coeff., mm^{-1}	24.7	27.6	29.7
Total no. of reflections	2889	1579	826
Independent reflections/R_{int}	229/0.0510	212/0.0696	190/0.0143
Reflections with $I \geq 3\sigma(I)/R_\sigma$	191/0.0168	175/0.0275	181/0.0122
Data/parameters	229/11	212/11	190/11
$R1/wR2$ for $I \geq 3\sigma(I)$	0.0177/0.0357	0.0208/0.0214	0.0105/0.0259
$R1/wR2$ for all data	0.0286/0.0393	0.0317/0.0221	0.0111/0.0260
Goodness-of-fit on F^2	1.23	1.16	1.03
Extinction scheme		Lorentzian isotropic [61]	
Extinction coefficient	160(50)	58(19)	350(20)
Diff. Fourier residues /e$^-$ Å^{-3}	−1.32/+1.01	−1.81/+1.40	−0.37/+1.06

The following discussion of the crystal structure and the interatomic distances is based on the single crystal data obtained for Y_2TiAl_3. As the crystal structure (Figure 3) can be derived from the cubic Laves phase ($MgCu_2$ type, $Fd\bar{3}m$), the structural relationship is fairly obvious. A group–subgroup scheme according to the Bärnighausen formalism for the structural relationship of $CeRh_2$ and Ce_2Rh_3Ga has been provided in the literature [40]. As in the $MgCu_2$-type structure, only two crystallographic positions are occupied (Mg on 8*a*, 0,0,0; Cu on 16*c*, 3/8, 3/8, 3/8) and no distinct ordering is possible. A *translationengleiche* transition of index 4 leads to the structure of Mg_2Ni_3Si in the rhombohedral crystal system and space group $R\bar{3}m$. This allows for a decoupling of the lattice parameters along with the possibility of atomic ordering (16*c* splits into 3*a* and 9*d*). In addition, Mg atoms (6*c*) gain a free *z* parameter allowing the adjustment of interatomic distances. A recent review article [47] summarizes the information on the superstructures of Laves phases.

Table 2. Atom positions and equivalent isotropic displacement parameters (pm^2) for Y_2TiAl_3, Gd_2TiAl_3, and Tb_2TiAl_3 determined from single crystal X-ray diffraction data. U_{eq} is defined as one-third of the trace of the orthogonalized U_{ij} tensor.

Atom	Wyckoff Position	x	y	z	U_{eq}
Y_2TiAl_3					
Y	6*c*	0	0	0.37244(4)	89(1)
Ti	3*a*	0	0	0	75(2)
Al	9*d*	1/2	0	1/2	88(3)
Gd_2TiAl_3					
Gd	6*c*	0	0	0.37333(3)	81(1)
Ti	3*a*	0	0	0	67(5)
Al	9*d*	1/2	0	1/2	84(7)
Tb_2TiAl_3					
Tb	6*c*	0	0	0.37348(1)	64(1)
Ti	3*a*	0	0	0	54(2)
Al	9*d*	1/2	0	1/2	69(3)

Table 3. Anisotropic displacement parameters (pm^2) for Y_2TiAl_3, Gd_2TiAl_3, and Tb_2TiAl_3 determined from single crystal X-ray diffraction data. Coefficients U_{ij} of the anisotropic displacement factor tensor of the atoms are defined by $-2\pi^2[(ha^*)^2U_{11} + \ldots + 2hka^*b^*U_{12}]$.

Atom	U_{11}	U_{22}	U_{33}	U_{12}	U_{13}	U_{23}
Y_2TiAl_3						
Y	86(2)	U_{11}	94(2)	43(1)	0	U_{13}
Ti	79(3)	U_{11}	66(4)	40(1)	0	U_{13}
Al	84(3)	86(4)	95(5)	43(2)	5(2)	10(1)
Gd_2TiAl_3						
Gd	79(2)	U_{11}	84(2)	40(1)	0	U_{13}
Ti	74(5)	U_{11}	54(9)	37(3)	0	U_{13}
Al	77(6)	80(11)	95(10)	40(5)	4(6)	8(13)
Tb_2TiAl_3						
Tb	62(1)	U_{11}	69(1)	31(1)	0	U_{13}
Ti	55(3)	U_{11}	52(4)	28(1)	0	U_{13}
Al	74(3)	68(5)	64(4)	34(2)	2(2)	5(3)

Table 4. Interatomic distances (pm) for Y_2TiAl_3, Gd_2TiAl_3, and Tb_2TiAl_3 determined from single crystal X-ray diffraction data. All distances of the first coordination spheres are listed. All standard uncertainties were less than 0.1 pm.

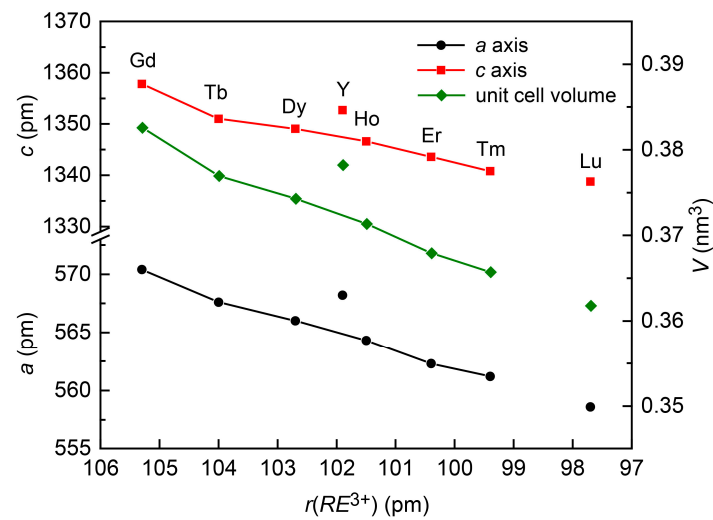|	**Y_2TiAl_3**				**Gd_2TiAl_3**				**Tb_2TiAl_3**		
Y:	3	Al	323.1	Gd:	3	Al	325.4	Tb:	3	Al	324.1
	3	Ti	332.3		6	Al	333.1		6	Al	331.3
	6	Al	332.4		3	Ti	333.8		3	Ti	332.1
	3	Y	344.7		1	Gd	344.1		1	Tb	342.2
	1	Y	345.1		3	Gd	346.8		3	Tb	345.1
Ti:	6	Al	278.8	Ti:	6	Al	279.9	Ti:	6	Al	278.6
	6	Y	332.3		6	Gd	333.8		6	Tb	332.1
Al:	2	Ti	278.8	Al:	2	Ti	279.9	Al:	2	Ti	278.6
	4	Al	284.1		4	Al	285.2		4	Al	283.7
	2	Y	323.1		2	Gd	325.4		2	Tb	324.1
	4	Y	332.4		4	Gd	333.1		4	Tb	331.3

Figure 1. Trigonal lattice parameters and unit cell volumes of the $RE_2\text{TiAl}_3$ (RE = Y, Gd–Tm, Lu) series ($\text{Mg}_2\text{Ni}_3\text{Si}$ type) plotted versus the ionic radii of the trivalent RE^{3+} cations. The connection between the data points is a guide to the eye.
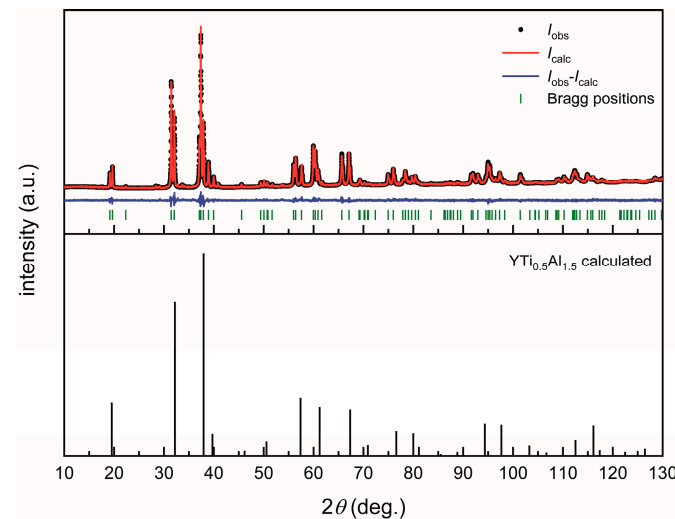

Figure 2. Rietveld refinement of Y_2TiAl_3 (**top**) in the trigonal $\text{Mg}_2\text{Ni}_3\text{Si}$-type structure in comparison with (**bottom**) the cubic MgCu_2-type structure.

Table 5. SEM-EDX data of the rhombohedral $RE_2\text{TiAl}_3$ series. Standard deviations are ± 2 at.-%.

Compound	RE (at.-%)	Ti (at.-%)	Al (at.-%)
Ideal composition	33.3	16.7	50.0
Single crystal data			
Y_2TiAl_3	36	16	48
Gd_2TiAl_3	34	16	50
Bulk sample data			
Er_2TiAl_3	36	14	50
Tm_2TiAl_3	32	16	52
Lu_2TiAl_3	37	15	48

Table 6. Lattice parameters of the rhombohedral RE_2TiAl_3 series (RE = Y, Gd–Tm, Lu), space group $R\bar{3}m$, $Z = 3$, Mg_2Ni_3Si type, determined by powder X-ray diffraction. [P] denotes powder data, [SC] single crystal data.

Compound	*a* (pm)	*c* (pm)	*V* (nm^3)
Y_2TiAl_3 [P]	568.29(4)	1353.0(1)	0.3784
Y_2TiAl_3 [SC]	568.22(7)	1352.9(2)	0.3783
Gd_2TiAl_3 [P]	569.81(5)	1359.6(2)	0.3823
Gd_2TiAl_3 [SC]	570.45(5)	1358.0(1)	0.3827
Tb_2TiAl_3 [P]	567.55(6)	1351.0(3)	0.3769
Tb_2TiAl_3 [SC]	567.39(6)	1352.4(2)	0.3771
Dy_2TiAl_3 [P]	565.90(6)	1349.1(2)	0.3742
Ho_2TiAl_3 [P]	564.86(3)	1347.5(1)	0.3723
Er_2TiAl_3 [P]	563.10(3)	1344.3(1)	0.3691
Tm_2TiAl_3 [P]	559.61(9)	1341.3(3)	0.3638
Lu_2TiAl_3 [P]	558.37(4)	1338.2(1)	0.3613

The tetrahedral entities in the cubic structure type are connected over all corners, forming a network, however, by only one crystallographic position. In rhombohedral Y_2TiAl_3, a splitting of this single position takes places, allowing full Ti/Al ordering in the empty [$TiAl_3$] tetrahedra. The Al atoms form 6^3 Kagomé nets, while the Ti atoms connect these nets over the triangles. In the cavities of this three-dimensional arrangement, the RE cations can be found. They form a distorted cubic diamond-type substructure, as highlighted in Figure 3. The coordination environments of the Ti and Al atoms are depicted in Figure 4. In the network, Ti–Al distances of 279 pm can be found, longer than the sum of the covalent radii (Ti + Al = 132 + 125 = 257 pm [60]), suggesting moderate bonding interactions. In the binary compounds TiAl (tetragonal CuAu type, $P4/mmm$ [62]) and Ti_3Al (hexagonal Mg_3Cd type, $P6_3/mmc$ [63]), interatomic distances of 283 and 286 + 289 pm are observed, respectively, while in the only thus far known ternary compound $Y_6Ti_4Al_{43}$ (hexagonal $Ho_6Mo_4Al_{43}$ type, $P6_3/mcm$ [64]), Ti–Al distances of 259–287 pm are found. The Y atoms in Y_2TiAl_3 are surrounded by 16 atoms in the shape of a Frank–Kasper polyhedra [65,66] according to $Y@Al_9Y_4Ti_3$ (Figure 4, top), while Ti and Al both exhibit icosahedra coordination environments (Figure 4, middle and bottom). The Ti atoms are surrounded octahedrally by the Al atoms along with six Y atoms ($Y@Al_6Y_6$), the Al atoms by four Al, two Ti, and six Y atoms ($Al@Al_4Ti_2Y_6$). The Y–Ti distances are 332 pm, while the Y–Al distances range between 323 and 332 pm, suggesting rather weak interactions when compared to the sum of the covalent radii (Y + Ti = 162 + 132 = 294 pm; Y + Al = 162 + 125 = 287 pm [60]). In YAl_2 (cubic $MgCu_2$ type, $Fd\bar{3}m$ [67,68]), heteroatomic Y–Al distances of 325 pm can be observed, which suggest rather low interactions. Since no binary phases in the system Y/Ti exist; only the comparison with $Y_6Ti_4Al_{43}$ [64] is possible. The shortest Y–Ti distance is 354 pm, also suggesting very weak to no bonding interactions, while Y–Al distances between 308 and 344 pm are observed. In Y_2TiAl_3, two different Y–Y distances (344.7 and 345.2 pm) are observed, due to the distortion of the cubic $MgCu_2$-type structure. In cubic YAl_2 [67,68], only one distance of 340 pm is found.

Attempts to extend the series of the RE_2TiAl_3 compounds to the larger elements (RE = La-Nd, Sm, Eu) were not successful. For the lanthanum compound, a synthesis under the same conditions as described above resulted in a mixture of the binary compounds $LaAl_2$ ($MgCu_2$ type), LaAl (CeAl type) and elemental titanium (Mg type). The refined powder pattern is shown in Figure S7 (Table S7).
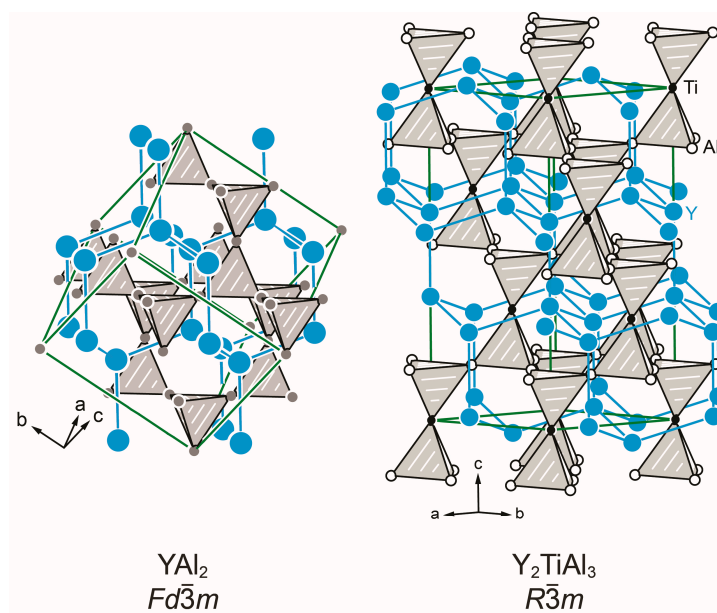
Figure 3. Unit cells of YAl_2 (**left**) and Y_2TiAl_3 (**right**). Yttrium, titanium, and aluminum atoms are depicted as blue, black, and open white circles, respectively. The empty $[Al_4]$ and $[TiAl_3]$ tetrahedra in YAl_2 and Y_2TiAl_3 and the diamond-related substructure formed by the Y atoms are highlighted.
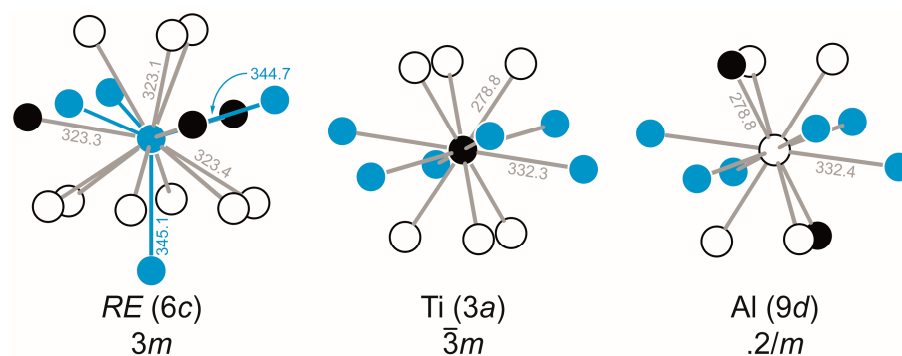

Figure 4. Coordination environments surrounding the Y, Ti, and Al atoms in the crystal structure of Y_2TiAl_3. Yttrium, titanium, and aluminum atoms are depicted as blue, black, and open white circles, respectively. Wyckoff sites, site symmetries, and interatomic distances (in pm) are given.

3.4. Physical Properties

The physical properties of the RE_2TiAl_3 series (Table 7; *RE* = Y, Gd–Tm, Lu) were determined by susceptibility and magnetization experiments. While Y_2TiAl_3 and Lu_2TiAl_3 exhibit Pauli paramagnetism, in line with their metallic character and the absence of (unpaired) *f*-electrons, all other compounds are paramagnetic. The temperature dependence of the magnetic susceptibility of Y_2TiAl_3 and Lu_2TiAl_3 is depicted in Figure 5. The susceptibility exhibits positive values over the whole investigated temperature region and reaches $\chi(300\ \text{K}) = +2.48(1) \times 10^{-4}$ emu mol^{-1} (Y_2TiAl_3) and $\chi(300\ \text{K}) = +2.14(1) \times 10^{-4}$ emu mol^{-1} (Lu_2TiAl_3), indicating that the Pauli paramagnetism overcompensates the intrinsic diamagnetism.
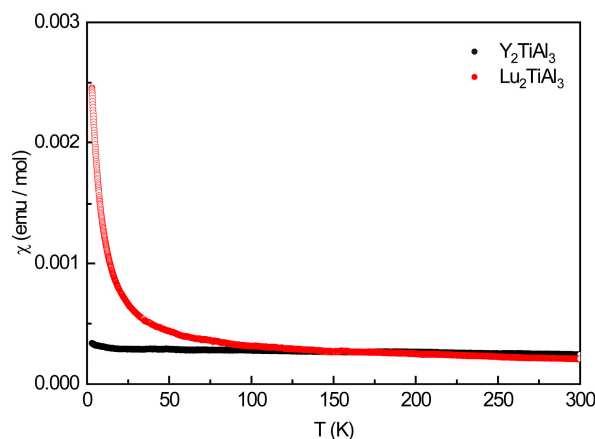
Figure 5. Temperature dependence of the magnetic susceptibility of Y_2TiAl_3 (black) and Lu_2TiAl_3 (red) measured with an applied external field of 10 kOe.

The magnetic data of Gd_2TiAl_3 is depicted in Figure 6. The ZFC (zero-field-cooled) investigations at high field (10 kOe) were conducted in the temperature range of 3–300 K and are shown in the top panel. From the inverse susceptibility, the effective magnetic moment was determined to $\mu_{eff} = 7.89(1)$ μ_B, well in line with the theoretical moment of $\mu_{eff,calc} = 7.94$ μ_B for a free Gd^{3+} cation. The paramagnetic Curie temperature is $\theta_P = +20.8(1)$ K, indicating dominant ferromagnetic interactions in the paramagnetic temperature regime. From the low-field 100 Oe ZFC/FC (zero-field-cooled/field-cooled) measurements, an antiferromagnetic ordering was derived with a Néel temperature of $T_N = 26.1(1)$ K. The rather strong bifurcation, along with the high residual magnetization, however, indicates that the investigated sample could contain ferromagnetic impurities. Samples of the same composition but from different batches exhibit a similar behavior. Therefore, homogeneity ranges within the samples are suspected. One impurity might be $GdAl_2$ [69], which exhibits ferromagnetic ordering below $T_C = 170$ K. Therefore, pure $GdAl_2$ cannot be the impurity but the solid solution $GdTi_xAl_{2-x}$ could be responsible for the magnetic behavior. Since these compounds crystallize in the cubic $MgCu_2$-type structure, trace impurities are invisible in the powder X-ray patterns, since the reflections overlap with those of rhombohedral Gd_2TiAl_3 (Figure 2). However, since ferromagnetic transitions are significantly stronger compared to antiferromagnetic ones (factor 1000 to 10,000), only traces of the respective impurity can be present. The magnetization isotherms (Figure 6, bottom) finally exhibit a steep increase already at low magnetic fields. This is an additional indication of the presence of ferromagnetic impurities. The 50 and 100 K isotherms are linear, as expected for a paramagnetic material; those measured at 3 and 10 K show a very weak curvature that could indicate an upcoming spin-reorientation at even higher fields. The comparatively low saturation magnetization of $\mu_{sat} = 3.98(1)$ μ_B reached at 3 K and 80 kOe also underlines a strong antiferromagnetic ground state. Similar effects have been observed, e.g., for $GdPtGe_2$ [70] or $Gd_3Pt_4Ge_6$ [71]. Usually, Gd intermetallics reach (nearly) the theoretical full saturation magnetization $\mu_{sat,theo} = 7$ μB according to $g_J \times J$, as seen, e.g., for $GdAl_2$ [72], Gd_3Al_2 [72], Gd_2RhAl_3 [14], or $GdPt_6Al_3$ [73].

Er_2TiAl_3 could be obtained in nearly pure form; the magnetic data are depicted in Figure 7. The effective magnetic moment was determined to be $\mu_{eff} = 9.73(1)$ μ_B and is slightly enhanced compared to the theoretical moment of $\mu_{eff,calc} = 9.58$ μ_B for a free Er^{3+} cation; the paramagnetic Curie temperature is $\theta_P = -6.5(1)$ K, indicating antiferromagnetic interactions in the paramagnetic temperature regime. An antiferromagnetic ordering was derived from the low-field zero-field-cooled measurements (Figure 7, middle) with a Néel temperature of $T_N = 17.6(1)$ K; however, again a bifurcation is visible, suggesting traces of ferromagnetic impurities. The magnetization isotherms (Figure 7, bottom) at 50 and 100 K isotherms are linear, as expected for a paramagnetic material; the ones measured at 3 and 10 K show an S-shape with a curvature that indicates a spin-reorientation at a critical field

of H_{crit} = 20.7(5) kOe, determined by the derived value of the 3 K isotherm. The saturation magnetization of μ_{sat} = 4.46(1) μ_B reaches 3 K and 80 kOe, which is below the expected value of $\mu_{sat,theo}$ = 9 μ_B according to $g_J \times J$.
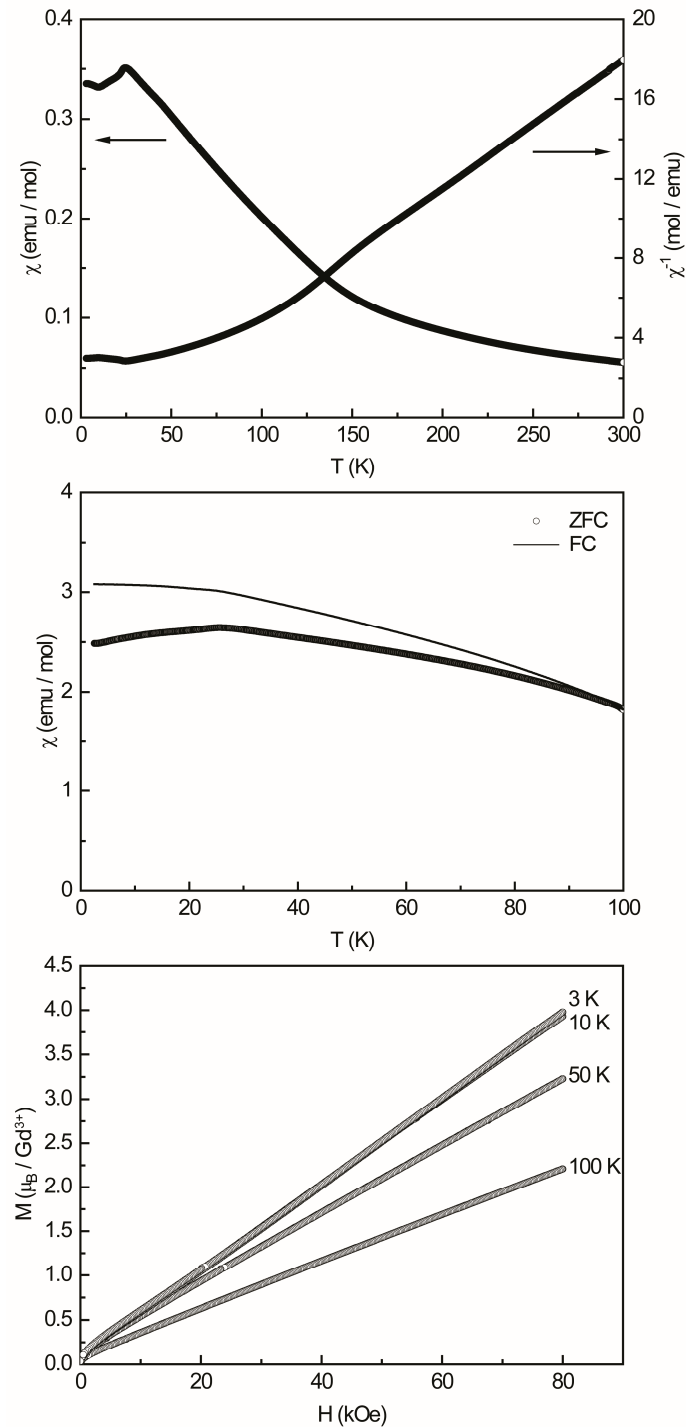

Figure 6. Magnetic data of Gd_2TiAl_3. (**top**) Temperature dependence of the magnetic and inverse magnetic susceptibility (χ and χ^{-1} data) measured with an applied external field of 10 kOe; (**middle**) zero-field-cooled/field-cooled (ZFC/FC) measurements measured with an applied external field of 100 Oe; (**bottom**) magnetization isotherms recorded at 3, 10, 50, and 100 K.
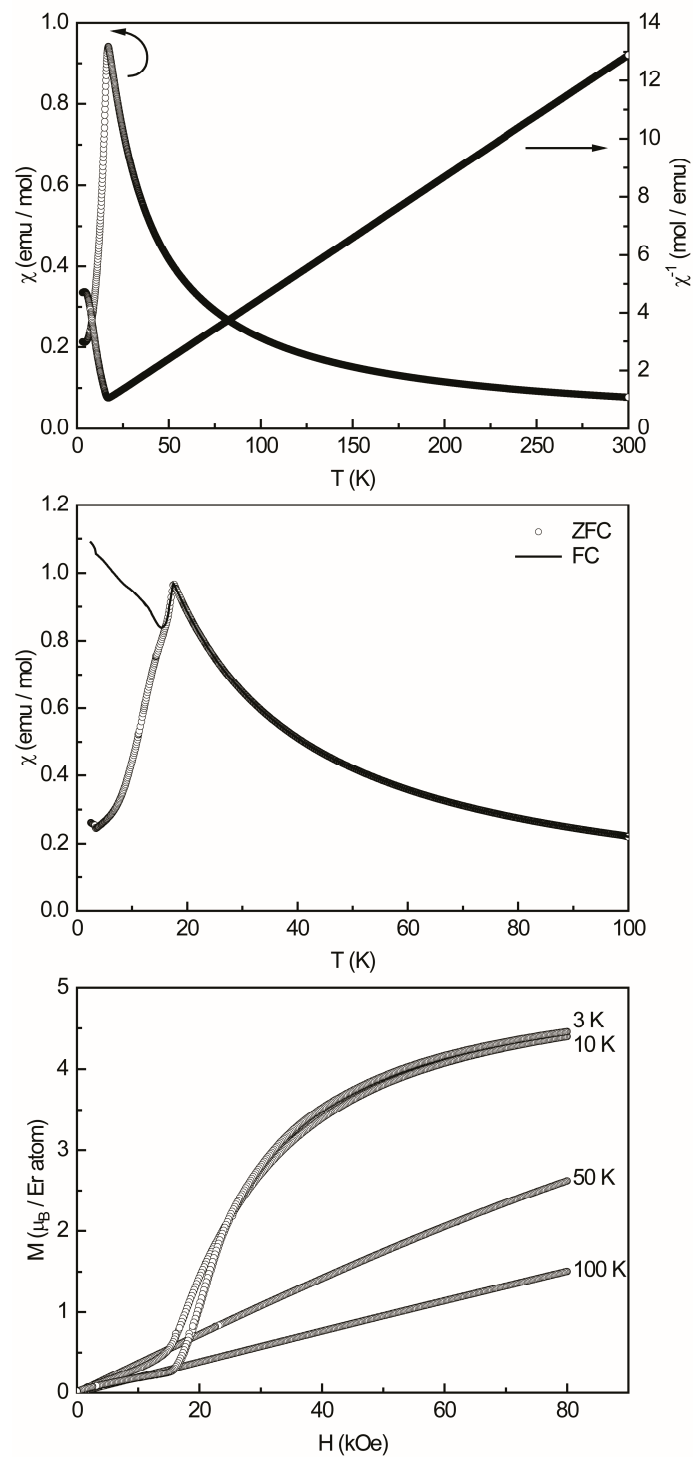
Figure 7. Magnetic data of Er_2TiAl_3. (**top**) Temperature dependence of the magnetic and inverse magnetic susceptibility (χ and χ^{-1} data) measured with an applied external field of 10 kOe; (**middle**) zero-field-cooled/field-cooled (ZFC/FC) measurements measured with an applied external field of 100 Oe; (**bottom**) magnetization isotherms recorded at 3, 10, 50, and 100 K.

Table 7. Physical properties of the RE_2TiAl_3 (RE = Y, Gd–Tm; Lu) series: T_N, Néel temperature; μ_{exp}, experimental magnetic moment; μ_{eff}, effective magnetic moment; θ_P, paramagnetic Curie temperature; μ_{sat}, experimental saturation magnetization; $g_J \times J$, theoretical saturation magnetization.

Compound	T_N (K)	μ_{exp} (μ_B)	μ_{eff} (μ_B)	θ_P (K)	μ_{sat} (μ_B per RE^{3+})	$g_J \times J$ (μ_B per RE^{3+})
Y_2TiAl_3	Pauli-paramagnetic, non-superconducting, χ(300 K) = +2.48(1) $\times 10^{-4}$ emu mol^{-1}					
Gd_2TiAl_3	26.1(1)	7.98(1)	7.94	+20.8(1)	3.98(1)	7
Tb_2TiAl_3	24.0(1)	10.04(1)	9.72	+31.7(1)	3.58(1)	9
Dy_2TiAl_3	26.1(1)	11.14(1)	10.65	−0.29(1)	7.98(1)	10
Ho_2TiAl_3	10.3(1)	10.85(1)	10.61	+0.72(1)	7.36(1)	10
Er_2TiAl_3	17.6(1)	9.73(1)	9.58	−6.5(1)	4.46(1)	9
Tm_2TiAl_3	10.8(1)	7.69(1)	7.61	−7.3(1)	3.46(1)	7
Lu_2TiAl_3	Pauli-paramagnetic, non-superconducting, χ(300 K) = +2.14(1) $\times 10^{-4}$ emu mol^{-1}					

4. Conclusions

In this paper, we present the synthesis as well as structural and magnetic characterization of the RE_2TiAl_3 series with RE = Y, Gd–Tm, and Lu. These compounds adopt the rhombohedral Mg_2Ni_3Si-type structure and are the first representations in the field of aluminum intermetallics. The crystal structures of Y_2TiAl_3, Gd_2TiAl_3, and Tb_2TiAl_3 have been refined from single crystal X-ray diffraction data and clearly indicate the formation of the rhombohedral structure. Powder X-ray diffraction experiments underline this observation as the diffraction patterns exhibit the expected splitting of reflections based on the transition from the cubic to the rhombohedral crystal system. Powder patterns of selected members of the series have been refined using the Rietveld method. All compounds have been characterized by magnetic susceptibility and magnetization experiments. While Y_2TiAl_3 and Lu_2TiAl_3 exhibit a nearly temperature independent behavior in line with the expected Pauli paramagnetism, the other compounds of the series show a stable trivalent oxidation state of the rare-earth atoms. All compounds exhibit antiferromagnetic transitions at lower temperatures; however, sometimes traces of ferromagnetic impurities can be observed. These originate from impurities that crystallize in the cubic $MgCu_2$-type structure and have to be considered solid solutions according to $RETi_xAl_{2−x}$. Even small traces of these compounds provide visible features in the magnetic data since ferromagnetic transitions are significantly stronger than antiferromagnetic ones. An identification of these impurities is impossible since their reflections overlap with those of the rhombohedral main phase. Finally, the valence electron concentration (VEC) also shows an intriguing feature. The title compounds exhibit a VEC of 19 e$^-$ (2× 3e$^-$ + 4e$^-$ + 3× 3e$^-$), while all other compounds that adopt the Mg_2Ni_3Si-type structure, including the prototype itself, exhibit VECs between 36 and 39. The stability of the aluminum representatives will be investigated by quantum-chemical calculations in the future.

Author Contributions: Conceptualization, O.J.; methodology, E.C.J.G., S.E., M.R., J.M.G. and L.S.; analysis, E.C.J.G., S.E., I.M.E., L.S. and O.J.; investigation, E.C.J.G., S.E., I.M.E., M.R., J.M.G. and L.S.; writing—original draft preparation, E.C.J.G. and M.R.; writing—review and editing, E.C.J.G. and O.J.; visualization, E.C.J.G.; supervision, O.J.; project administration, O.J.; funding acquisition, O.J. All authors have read and agreed to the published version of the manuscript.

Conflicts of Interest: The authors declare no conflict of interest.

References

1. Paufler, P.; Gustav, E.R. Schulze's pioneering work on Laves phases. *Z. Kristallogr.* **2006**, *221*, 311. [CrossRef]
2. Fischer, W.; Fritz, H. Laves—An ideal for generations. *Z. Kristallogr.* **2006**, *221*, 305. [CrossRef]
3. Parthé, E.; Fritz, H. Laves—100 years young. *Z. Kristallogr.* **2006**, *221*, 301. [CrossRef]
4. Villars, P.; Cenzual, K. (Eds.) *Pearson's Crystal Data: Crystal Structure Database for Inorganic Compounds*; (release 2022/23); ASM International®: Materials Park, OH, USA, 2023.
5. Laves, F.; Witte, H. Der Einfluß von Valenzelektronen auf die Kristallstruktur ternärer Magnesiumlegierungen. *Metallwirtsch. Metallwiss. Metalltech.* **1936**, *15*, 840–842.
6. Gschneidner, K.A., Jr.; Pecharsky, V.K. Binary rare earth Laves phases—An overview. *Z. Kristallogr.* **2006**, *221*, 375–381. [CrossRef]
7. Fukui, H.; Hirao, N.; Ohishi, Y.; Baron, A.Q.R. Compressional behavior of solid $NeHe_2$ up to 90 GPa. *J. Phys. Condens. Matter* **2010**, *22*, 095401. [CrossRef] [PubMed]
8. Dewaele, A.; Rosa, A.D.; Guignot, N. Argon-neon binary diagram and $ArNe_2$ Laves phase. *J. Chem. Phys.* **2019**, *151*, 124708. [CrossRef]
9. Ji, C.; Goncharov, A.F.; Shukla, V.; Jena, N.K.; Popov, D.; Li, B.; Wang, J.; Meng, Y.; Prakapenka, V.B.; Smith, J.S.; et al. Stability of $Ar(H_2)_2$ to 358 GPa. *Proc. Natl. Acad. Sci. USA* **2017**, *114*, 3596–3600. [CrossRef]
10. Laniel, D.; Weck, G.; Loubeyre, P. $Xe(N_2)_2$ compound to 150 GPa: Reluctance to the formation of a xenon nitride. *Phys. Rev. B* **2016**, *94*, 174109. [CrossRef]
11. Komura, Y.; Kitano, Y. Long-period stacking variants and their electron-concentration dependence in the Mg-base Friauf-Laves phases. *Acta Crystallogr.* **1977**, *B33*, 2496–2501. [CrossRef]
12. Witte, H. Untersuchungen im System Magnesium-Kupfer-Silicium mit besonderer Berücksichtigung des Schnittes $MgCu_2$-$MgSi_2$. *Z. Angew. Mineral.* **1938**, *1*, 255–268.
13. Mishra, T.; Hoffmann, R.-D.; Schwickert, C.; Pöttgen, R. Structure Refinement and Magnetic Properties of Ce_2RuAl_3 and a Group-Subgroup Scheme for $Ce_5Ru_3Al_2$. *Z. Naturforsch.* **2011**, *66b*, 771–776. [CrossRef]
14. Eustermann, F.; Stegemann, F.; Gausebeck, S.; Janka, O. Structural and Magnetic Investigations of the Pseudo Ternary RE_2TAl_3 series (RE = Sc, Y, La–Nd, Sm, Gd–Lu; T = Ru, Rh, Ir)—Size Dependent Formation of Two Different Structure Types. *Z. Naturforsch.* **2018**, *73b*, 819–830. [CrossRef]
15. Blazina, Z.; Ban, Z. The Crystal Structures of U_2Cu_3Al and $UCuAl_2$, and their Relationship with Some Other Phases in the System U-Cu-Al. *Z. Naturforsch.* **1981**, *35b*, 1162–1165.
16. Huneau, B.; Rogl, P.; Zeng, K.; Schmid-Fetzer, R.; Bohn, M.; Bauer, J. The ternary system Al–Ni–Ti Part I: Isothermal section at 900 °C; Experimental investigation and thermodynamic calculation. *Intermetallics* **1999**, *7*, 1337–1345. [CrossRef]
17. Zelinskii, A.V.; Fedorchuk, A.O.; Zelinska, O.Y. Synthesis and crystal structure of the compounds $UMn_{1.43}Ga_{0.57}$ and U_2Fe_3Ga. *Visn. Lviv. Derzh. Univ. Ser. Khim.* **2013**, *54*, 92–97.
18. Sichevych, O.; Prots, Y.; Schnelle, W.; Schmidt, M.; Grin, Y. Crystal structure of dieuropium trigallium iridium, Eu_2Ga_3Ir. *Z. Kristallogr. NCS* **2006**, *221*, 263–264. [CrossRef]
19. Mykhalichko, O.; Gladyshevskii, E.I.; Hlukhyy, V.; Fässler, T.F. Synthesis and crystal structure of the compound $Nb_2Cu_{1.10}Ga_{2.90}$. *Visn. Lviv. Derzh. Univ. Ser. Khim.* **2009**, *50*, 89–93.
20. Myakush, O.R.; Fedorchuk, A.A. Crystal structure and electrical properties of HoRuGa compound. *Visn. Lviv. Derzh. Univ. Ser. Khim.* **2004**, *44*, 62–66.
21. Yan, X.L.; Chen, X.-Q.; Grytsiv, A.; Witusiewicz, V.T.; Rogl, P.; Podloucky, R.; Giester, G. On the ternary Laves phases {Sc,Ti}$_2M_3$Si (M = Cr, Mn, Fe, Co, Ni) with $MgZn_2$-type. *J. Alloys Compd.* **2007**, *429*, 10–18. [CrossRef]
22. Kotur, B.Y. Crystal structure of Sc_2M_3Si (where M = Fe, Co, Ni) compounds. *Dopov. Akad. Nauk Ukr. RSR* **1977**, *A39*, 164–165.
23. Bardos, D.I.; Gupta, K.P.; Beck, P.A. Ternary Laves Phases with Transition Elements and Silicon. *Trans. Metall. Soc. AIME* **1961**, *221*, 1087–1088.
24. Henriques, M.S.; Berthebaud, D.; Lignie, A.; El Sayah, Z.; Moussa, C.; Tougait, O.; Havela, L.; Gonçalves, A.P. Isothermal section of the ternary phase diagram U–Fe–Ge at 900 °C and its new intermetallic phases. *J. Alloys Compd.* **2015**, *639*, 224–234. [CrossRef]

25. Hoffmann, R.-D.; Pöttgen, R.; Chevalier, B.; Gaudin, E.; Matar, S.F. The ternary germanides UMnGe and U_2Mn_3Ge. *Solid State Sci.* **2013**, *21*, 73–80. [CrossRef]

26. Soudé, A.; Tougait, O.; Pasturel, M.; Kaczorowski, D.; Noël, H.; Roisnel, T. Characterization of the novel intermetallic compounds U_2Co_3Ge, $U_6Co_{12}Ge_4$ and $U_6Co_{12}Ge_4C$. *J. Alloys Compd.* **2011**, *509*, 5447–5452. [CrossRef]

27. Henriques, M.S.; Tougait, O.; Noel, H.; Pereira, L.C.J.; Waerenborgh, J.C.; Gonçalves, A.P. Evidence of uranium magnetic ordering on U_2Fe_3Ge. *Solid State Commun.* **2008**, *148*, 159–162. [CrossRef]

28. Teslyuk, M.Y.; Gladyshevskii, E.I. Crystal structure of $MnCu_{1.5}Ge_{0.5}$ ternary compound. *Visn. Lviv. Derzh. Univ. Ser. Khim.* **1963**, *6*, 42–45.

29. Kuz'ma, Y.B.; Gladyshevskii, E.I. Crystal structure of the compound Mn_2Co_3Ge. *Dopov. Akad. Nauk Ukr. RSR* **1963**, *A25*, 205–208.

30. Gladyshevskii, E.I.; Krypyakevych, P.I.; Teslyuk, M.Y. Crystal structure of the ternary phase Cu_4MgSn. *Dokl. Akad. Nauk. SSSR* **1952**, *85*, 81–84.

31. Zaremba, V.I.; Baranyak, V.M.; Kalychak, Y.M. Crystal structure of the RNi_4In compounds. *Visn. Lviv. Derzh. Univ. Ser. Khim.* **1984**, *25*, 18–19.

32. Felner, I. Magnetic properties of $RAuNi_4$ rare earth compounds. *Solid State Commun.* **1977**, *21*, 267–268. [CrossRef]

33. Dwight, A.E. Crystal structure of $RENi_4Au$ compounds and unitcell constants in the YCo_5-YNi_5-YCu_5 series. *J. Less-Common Met.* **1975**, *43*, 117–120. [CrossRef]

34. Takeshita, T.; Malik, S.K.; Wallace, W.E. Crystal structure of RCu_4Ag and RCu_4Al (R = Rare Earth) intermetallic compounds. *J. Solid State Chem.* **1978**, *23*, 225–229. [CrossRef]

35. Kaneko, T.; Arai, S.; Abe, S.; Kamigaki, K. Magnetic properties of cubic $RAuCu_4$ (R = Gd, Tb, Dy, Ho and Er) intermetallic compounds. *J. Phys. Soc. Jpn.* **1986**, *55*, 4441–4447. [CrossRef]

36. Seidel, S.; Pöttgen, R. $Yb_6Ir_5Ga_7$—A $MgZn_2$ Superstructure. *Z. Anorg. Allg. Chem.* **2017**, *643*, 261–265. [CrossRef]

37. Eustermann, F.; Pominov, A.; Pöttgen, R. Rare Earth (*RE*) Gallides with Closely Related Compositions: *RE*IrGa and $RE_6Ir_5Ga_7$. *Z. Anorg. Allg. Chem.* **2018**, *644*, 1297–1303. [CrossRef]

38. Eustermann, F.; Stegemann, F.; Radzieowski, M.; Janka, O. Intermetallic $RE_6T_5Al_7$ Phases (*RE* = Sc, Y, Ce–Nd, Sm, Gd–Lu, *T* = Ru, Ir)—Diversity in their Magnetic, Magnetocaloric and Critical Properties. *Inorg. Chem.* **2019**, *58*, 16211–16226. [CrossRef]

39. Noréus, D.; Eriksson, L.; Göthe, L.; Werner, P.E. Structure determination of Mg_2SiNi_3. *J. Less-Common Met.* **1985**, *107*, 345–349. [CrossRef]

40. Seidel, S.; Janka, O.; Benndorf, C.; Mausolf, B.; Haarmann, F.; Eckert, H.; Heletta, L.; Pöttgen, R. Ternary rhombohedral Laves phases RE_2Rh_3Ga (*RE* = Y, La–Nd, Sm, Gd–Er). *Z. Naturforsch.* **2017**, *72b*, 289–303. [CrossRef]

41. Cenzual, K.; Chabot, B.; Parthé, E. Y_2Rh_3Ge, a rhombohedral substitution variant of the $MgCu_2$ type. *J. Solid State Chem.* **1987**, *70*, 229–234. [CrossRef]

42. Lipatov, A.; Gribanov, A.; Grytsiv, A.; Safronov, S.; Rogl, P.; Rousnyak, J.; Seropegin, Y.; Giester, G. The ternary system cerium–rhodium–silicon. *J. Solid State Chem.* **2010**, *183*, 829–843. [CrossRef]

43. Kaczorowski, D.; Lipatov, A.; Gribanov, A.; Seropegin, Y. Low-temperature magnetic and electrical transport properties of some ternary Ce–Rh–Si compounds. *J. Alloys Compd.* **2011**, *509*, 6518–6521. [CrossRef]

44. Vernière, A.; Lejay, P.; Bordet, P.; Chenavas, J.; Brison, J.P.; Haen, P.; Boucherle, J.X. Crystal structures and physical properties of some new ternary compounds U_2T_3X (*T* = Ru, Os; *X* = Si, Ge). *J. Alloys Compd.* **1994**, *209*, 251–255. [CrossRef]

45. Morozkin, A.V. New ternary compounds in the Sm–Rh–Ge system. *J. Alloys Compd.* **2004**, *385*, L1–L2. [CrossRef]

46. Doverbratt, I.; Ponou, S.; Lidin, S. Ca_2Pd_3Ge, a new fully ordered ternary Laves phase structure. *J. Solid State Chem.* **2013**, *197*, 312–316. [CrossRef]

47. Gießelmann, E.; Pöttgen, R.; Janka, O. Laves phases: Superstructures induced by coloring and distortions. *Z. Anorg. Allg. Chem.* **2023**, e202300109. [CrossRef]

48. Janka, O. *Metallic Light-Weight Alloys: Al, Ti, Mg*; Pöttgen, R., Jüstel, T., Strassert, C., Eds.; De Gruyter: Berlin, Germany; Boston, MA, USA, 2022.

49. Massalski, T.B.; Okamoto, H.; Subramanian, P.R.; Kacprzak, L. *Binary Alloy Phase Diagrams*, 2nd ed.; ASM International: Materials Park, OH, USA, 1990.

50. Okamoto, H. Al-Ti (aluminum-titanium). *J. Phase Equilibria* **1993**, *14*, 120–121. [CrossRef]

51. Raghavan, V. Al-Ti-V (Aluminum-Titanium-Vanadium). *J. Phase Equilibria Diffus.* **2005**, *26*, 276–279. [CrossRef]

52. Batalu, D.; Coşmeleaţă, G.; Aloman, A. Critical analysis of the Ti-Al phase diagrams. *U.P.B. Sci. Bull. Ser. B* **2006**, *68*, 77–90.

53. Schuster, J.C.; Palm, M. Reassessment of the binary Aluminum-Titanium phase diagram. *J. Phase Equilibria Diffus.* **2006**, *27*, 255–277. [CrossRef]

54. Peters, M.; Hemptenmacher, J.; Kumpfert, J.; Leyens, C. *Structure and Properties of Titanium and Titanium Alloys in Titanium and Titanium Alloys: Fundamentals and Applications*; Wiley-VCH Verlag GmbH: Weinheim, Germany, 2003.

55. Sauthoff, G. *Intermetallics in Ullmann's Encyclopedia of Industrial Chemistry*; Wiley-VCH Verlag GmbH: Weinheim, Germany, 2012.

56. Pöttgen, R.; Gulden, T.; Simon, A. Miniaturisierte Lichtbogenapperatur für den Laborbedarf. *GIT Labor-Fachz.* **1999**, *43*, 133–136.

57. Palatinus, L.; Chapuis, G. SUPERFLIP—A computer program for the solution of crystal structures by charge flipping in arbitrary dimensions. *J. Appl. Crystallogr.* **2007**, *40*, 786–790. [CrossRef]

58. Petříček, V.; Dušek, M.; Palatinus, L. (Eds.) *The Crystallographic Computing System*; JANA 2006; Institute of Physics of the Czech Academy of Sciences: Praha, Czech Republic, 2006.

59. Petříček, V.; Dušek, M.; Palatinus, L. Crystallographic Computing System JANA2006: General features. *Z. Kristallogr.* **2014**, *229*, 345–352. [CrossRef]

60. Emsley, J. *The Elements*; Clarendon Press: Oxford, UK; Oxford University Press: New York, NY, USA, 1998.

61. Becker, P.J.; Coppens, P. Extinction within the limit of validity of the Darwin transfer equations. I. General formalism for primary and secondary extinction and their applications to spherical crystals. *Acta Crystallogr.* **1974**, *A30*, 129–147. [CrossRef]

62. Duwez, P.E.; Taylor, J.L. Crystal Structure of TiAl. *Trans. Am. Inst. Min. Metall. Pet. Eng.* **1952**, *194*, 70–71. [CrossRef]

63. Ence, E.; Margolin, H. Compounds in the Titanium-Rich Region of the Ti-Al System. *Trans. Am. Inst. Min. Metall. Pet. Eng.* **1957**, *209*, 484–485. [CrossRef]

64. Niemann, S.; Jeitschko, W. Ternary aluminides $A_6T_4Al_{43}$ with A = Y, Nd, Sm, Gd-Lu, Th, U and T = Cr, Mo, W. *Z. Metallkd.* **1994**, *85*, 345–349.

65. Frank, F.C.; Kasper, J.S. Complex alloy structures regarded as sphere packings. II. Analysis and classification of representative structures. *Acta Crystallogr.* **1959**, *12*, 483–499. [CrossRef]

66. Frank, F.C.; Kasper, J.S. Complex alloy structures regarded as sphere packings. I. Definitions and basic principles. *Acta Crystallogr.* **1958**, *11*, 184–190. [CrossRef]

67. Compton, V.B.; Matthias, B.T. Laves phase compounds of rare earths and hafnium with noble metals. *Acta Crystallogr.* **1959**, *12*, 651–654. [CrossRef]

68. Gießelmann, E.C.J.; Engel, S.; Kostusiak, W.; Zhang, Y.; Herbeck-Engel, P.; Kickelbick, G.; Janka, O. Raman and NMR spectroscopic and theoretical investigations of the cubic Laves-phases $REAl_2$ (RE = Sc, Y, La, Yb, Lu). *Dalton Trans.* **2023**, *52*, 3391–3402. [CrossRef] [PubMed]

69. Zhou, G.F.; Bakker, H. Mechanically induced structural and magnetic changes in the $GdAl_2$ Laves phase. *Phys. Rev. B* **1995**, *52*, 9437–9445. [CrossRef] [PubMed]

70. Janka, O.; Hoffmann, R.D.; Heying, B.; Pöttgen, R. Structural phase transitions in $YPtGe_2$ and $GdPtGe_2$. *Dalton Trans.* **2018**, *47*, 6075–6088. [CrossRef] [PubMed]

71. Eustermann, F.; Eilers-Rethwisch, M.; Renner, K.; Hoffmann, R.-D.; Pöttgen, R.; Janka, O. Magnetic properties of the germanides $RE_3Pt_4Ge_6$ (RE = Y, Pr, Nd, Sm, Gd–Dy). *Z. Naturforsch.* **2017**, *72b*, 855–864. [CrossRef]

72. Staliński, B.; Pokrzywnicki, S. Magnetic Properties of Gadolinium-Aluminium Intermetallic Compounds. *Phys. Status Solidi B* **1966**, *14*, K157–K160. [CrossRef]

73. Eustermann, F.; Stegemann, F.; Renner, K.; Janka, O. Platinum Triangles in the Pt/Al Framework of the Intermetallic $REPt_6Al_3$ (RE = Ce-Nd, Sm, Gd, Tb) Series. *Z. Anorg. Allg. Chem.* **2017**, *643*, 1836–1843. [CrossRef]